Sliding-Mode Observer-based Navigation Algorithms and Artificial Potential Fields for Space Proximity Operations

AAS 21-685

SLIDING-MODE OBSERVER-BASED NAVIGATION ALGORITHMS AND ARTIFICIAL POTENTIAL FIELDS FOR SPACE PROXIMITY OPERATIONS

Davide Celestini[1], Martina Ciavola[1] and Elisa Capello[2] ⋕

This paper proposes Sliding-Mode Observer (SMO) and Artificial Potential Field (APF) as Navigation and Guidance algorithms for space applications. Both robust linear first-order and Super-Twisting SMOs are designed for performing sensor filtering measurements. Optical cameras and accelerometers are considered as sensors. A comparison with an Extended Kalman Filter (EFK) is proposed, in order to show the effectiveness of SMOs as alternative navigation algorithms. Harmonic 3D functions for the APF algorithm are proposed to manage issues related to the presence of local minima. Moreover, the repulsive field is changed for including moving targets and obstacles. Finally, the effectiveness of these algorithms is shown through numerical simulations, achieving results suitable for autonomous Rendezvous and Proximity Operations.

INTRODUCTION

During the design and the implementation of on-board space software, uncertainties, disturbances or measurement signals corrupted by noise usually arise and filtering approaches based on Kalman filter are implemented on-board. These filtering approaches can be easily found in literature since they are considered very effective, computationally efficient and they guarantee a simple on-line implementation.[1,2] In this paper, Sliding-Mode based Observers (SMO) are designed for estimating positions and linear velocities during a Space Proximity Operation, in order to perform sensor data fusion. Moreover, a first-order and a second order Super-Twisting (STW) SMOs are considered to automatically select the best estimation techniques in accordance to the available sensors.

SMO can be considered as an alternative to the problem of observation of perturbed systems and different applications have already been studied, not only in space environment.[3–5] In Reference 6 a SMO has been implemented to achieve sensorless drive and estimate position and velocity of a permanent magnet synchronous motor. As detailed in this work, the use of a SMO-based strategy appears to be more robust than classical methods, when parametric variations and uncertainties are included. Another application has been studied in the observation of a freeway traffic system in Reference 7. In this study, the estimation of traffic state variables, like density or speed, has been studied with the second order Super-Twisting (STW) SMO method also compared with Extended Kalman Filter (EKF). The results show robustness, stability and convergence to the solution in finite time. In space applications, a comparison between high-order SMO and EKF has been proposed in

*[1] D. Celestini and M. Ciavola are with Department of Mechanical and Aerospace Engineering, davide.celestini@polito.it, martina.ciavola@polito.it

†[2] E. Capello is with Department of Mechanical and Aerospace Engineering, Politecnico di Torino, CNR-IEIIT, Torino, Italy elisa.capello@polito.it

Reference 8 via Montecarlo simulations in the homing missile guidance system. The combination of high-order SMO and Proportional Navigation (PN) algorithm show robustness against noise and performance comparable to the optimal EKF law. Furthermore, different methods for spacecraft attitude and rate estimation using variable structure systems theory are presented in Reference 9. In this work, both a linearized decoupled SMO and a low-pass filtering of SMO are described, showing the estimation even in presence of large quantities of uncertainty in the inertia matrix and disturbance in the input torques.

The estimation algorithms are usually combined with guidance or control algorithms to perform autonomous rendezvous maneuver and proximity operations of two spacecraft in presence of obstacles. In the aerospace field, the rendezvous maneuver consists in a series of operations between two spacecraft, a passive Target and an active Chaser.[10] An analytical method and a computational-efficient algorithm is proposed in this paper to reach the Target in a safe way and to rapidly adjust the trajectory when the Chaser is close to an obstacle. Artificial Potential Field (APF) algorithms offer interesting features, such as *online* collision-free paths computation capabilities. The intuitive founding idea of the algorithm is to build an artificial potential field as sum of different fields with global maximum and minimum points to represent respectively obstacles and goal points. In such way, a robot moving inside the field would be naturally attracted towards the goal point by the attractive field, and away from obstacles by the repulsive one. The effectiveness of this method has already been shown in other works, including robotic and space applications.[11–14] However, one of the algorithm main issues is the (potential) presence of *local minima*, which could cause an unplanned stop of the Chaser motion. In literature, some solutions are proposed to overcome this issue.[15,16]

In our work, the main key features are: (i) a method for performing data fusion with different SMOs, (ii) their combination and management in the navigation algorithms, to select the best strategy in accordance to the available sensors, and (iii) a guidance algorithm based on APF harmonic 3D function. A mathematical proof of the local minimum avoidance is provided thanks to the definition of harmonic functions. Some changes in the APF repulsive and attractive fields are proposed to deal with moving targets and obstacles, starting from Reference 17 and 14.

The paper is organized as follows. The second section introduces the system dynamics. In the third section Sliding-Mode based Observer algorithms are presented. In the fourth section the APF technique is introduced, with a focus on the contribution of this paper, while the fifth section presents the Sliding-Mode Controller selected to track the APF streamlines. Simulation results are presented in the sixth section. Finally, conclusions are drawn in the last section.

SPACECRAFT DYNAMICS

The mathematical model used to describe relative orbital dynamics of the Chaser spacecraft (S/C) w.r.t. a Target moving on a circular orbit during Proximity Operations consists of the set of linear differential equations shown in Reference 10 and known as Hill's equations.

$$\begin{aligned} \ddot{\mathrm{x}} - 2\omega\dot{\mathrm{z}} &= \frac{1}{m_c}F_x \\ \ddot{\mathrm{y}} + 2\omega^2\mathrm{y} &= \frac{1}{m_c}F_y \\ \ddot{\mathrm{z}} - 3\omega^2\mathrm{z} + 2\omega\dot{\mathrm{x}} &= \frac{1}{m_c}F_z \end{aligned} \tag{1}$$

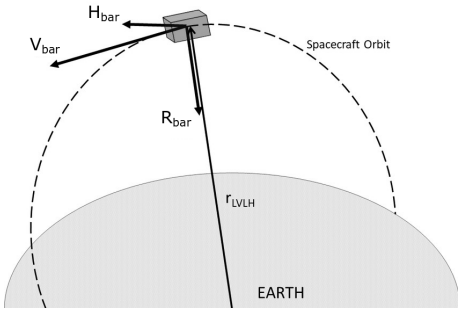

Figure 1: **Target LVLH frame.**[13]

where $r = [\mathrm{x}, \mathrm{y}, \mathrm{z}]^{\mathrm{T}} \in \mathbb{R}^3$ represents the Chaser relative position vector in the Target Local Vertical/Local Horizontal (LVLH) frame, ω is the orbital angular velocity of the reference LVLH frame (centered in the Target), $v = [\dot{\mathrm{x}}, \dot{\mathrm{y}}, \dot{\mathrm{z}}]^T = [v_x, v_y, v_z]^T \in \mathbb{R}^3$ is the Chaser velocity vector and m_c is the Chaser mass. $V_{bar}, H_{bar}, R_{bar}$ are the axes of the LVLH frame, as in Figure 1. $F = [F_x, F_y, F_z]^T \in \mathbb{R}^3$ represents the forces acting on the Chaser.

This linear set of equations can be easily rewritten in the classic state-space representation as

$$\begin{aligned} \dot{x}(t) &= Ax(t) + Bu(t) \\ y(t) &= Cx(t) \end{aligned} \tag{2}$$

with $x \in \mathbb{R}^n$, $u \in \mathbb{R}^m$ and $y \in \mathbb{R}^p$ the state, the input and the controlled output vectors, while $A \in \mathbb{R}^{n \times n}$, $B \in \mathbb{R}^{n \times m}$ and $C \in \mathbb{R}^{p \times n}$ represent the state, control and output matrices. The linearized model can be easily obtained from Eq. (1).

SLIDING MODE OBSERVERS FOR NAVIGATION

As briefly explained before, SMO observers are a valid alternative as filtration strategies with respect to Kalman filtering, for two main reasons: (i) they guarantee finite-time convergence and (ii) no knowledge about noise statistics is strictly required. Linear SMOs are simple observers in which the solution converges in finite time due to the discontinuity introduced by the switching error injection term. These observers can be easily implemented but they cannot always guarantee robustness to external disturbances. Moreover, an important drawback is the chattering behaviour, affected by the update frequency of the algorithms and the parameter tuning. For this reason, a robust linear SMO with unknown inputs is proposed. Nevertheless, high-order SMOs have high precision and robust behaviour with respect to parametric uncertainties, hence they can be efficiently used for state observation. Furthermore, they can be applied for disturbance reconstruction with a complete or only partial knowledge of the system model. Instead of linear SMO, high-order SMOs and in particular STW-SMO, are not strongly affected by chattering so they can better estimate the system states. In this paper two strategies are analyzed: a Linear Robust SMO and a second-order STW-SMO. Both the observers are detailed in Reference 18 and an analysis of the two algorithms is shown in the following sections.

Linear Robust SMO

The first algorithm presented is shown in Reference 18 and analyzes the problem of robust state estimation for systems with bounded matched uncertainties starting from the definition of first-order

linear observers. Considering the nominal linear system in Eq. (2), it is assumed that C matrix has full row rank. The first-order observer can be expressed as

$$\begin{aligned} \dot{\hat{x}}(t) &= A\hat{x}(t) + Bu(t) + G_n\nu \\ \hat{y}(t) &= C\hat{x}(t) \end{aligned} \tag{3}$$

where $(\hat{x}, \hat{y})$ are the estimates of (x, y) and ν is a discontinuous injection term. Defining the state and the output estimation errors respectively as $e(t) := \hat{x}(t) - x(t)$ and $e_y := \hat{y}(t) - y(t)$, and considering ρ as a positive scalar, the term ν is defined as

$$\nu_i = \rho \operatorname{sign}(e_{y,i}), \qquad i = 1, 2, \ldots, p \tag{4}$$

and it is designed to be discontinuous with respect to the sliding surface $\mathcal{S}$, to force the trajectories of $e(t)$ onto $\mathcal{S}$ in finite time. The gain matrix G_n has the structure $G_n = [L; -I_p]$, where $L \in \mathbb{R}^{(n-p)\times p}$ is designed by the user, in accordance to the requirements. Thus, the error system is given by

$$\dot{e}(t) = Ae(t) + G_n\nu \tag{5}$$

More details of linear observer can be found in Reference 18.

A robust version of this first-order linear SMO is implemented for the space application, in which bounded uncertainties or disturbances are considered through the known matrix B. Consider the system

$$\begin{aligned} \dot{x}(t) &= Ax(t) + Bu(t) + Bf(t, y, u) \\ y(t) &= Cx(t) \end{aligned} \tag{6}$$

where $f : \mathbb{R}_+ \times \mathbb{R}^p \times \mathbb{R}^m \mapsto \mathbb{R}^m$ represents combined uncertainties or nonlinearities. The function is unknown but bounded, so $\|f(t, y, u)\| \leq \rho(t, y, u)$, where $\rho(\cdot)$ are the known bounds. Consider an observer of the following form

$$\dot{\hat{x}}(t) = A\hat{x}(t) + Bu(t) - GCe(t) - P^{-1}C^T F^T \nu, \tag{7}$$

where $e(t)$ represents the error and can be defined as $e(t) = \hat{x}(t) - x(t)$. The gain matrix G and the symmetric positive definite matrix $P \in \mathbb{R}^{n\times n}$ satisfy the Linear Matrix Inequality (LMI) expressed as

$$PA_0 + A_0^T P \leq 0 \tag{8}$$

where $A_0 := A - GC$, and also satisfy the structural constraint

$$PB = (FC)^T \tag{9}$$

with $F \in \mathbb{R}^{m\times p}$. The discontinuous scaled unit vector term can now be written as

$$\nu = \rho(t, y, u) \operatorname{sign}(FCe(t)). \tag{10}$$

According to the definition of B starting from Eq. (1), we assume that all the states are measurable, both positions and velocities, in order to solve the described LMI. Therefore C is the identity matrix and $p = n$.

Super-Twisting SMO

As previously underlined and as for the first-order SMO, the Super-Twisting SMO is a second-order observer, with finite-time convergence. As stated in Reference 18, considering the eventually non-linear dynamic system described as

$$\begin{aligned} \dot{x}_1(t) &= x_2(t) \\ \dot{x}_2(t) &= f(t, x_1, x_2, u) + \xi(t, x_1, x_2, u) \end{aligned} \tag{11}$$

where $\xi(t, x_1, x_2, u)$ is an external disturbance, the Super-Twisting observer has the form

$$\begin{aligned} \dot{\hat{x}}_1(t) &= \hat{x}_2(t) + z_1 \\ \dot{\hat{x}}_2(t) &= f(t, x_1, \hat{x}_2, u) + z_2 \end{aligned} \tag{12}$$

where $(\hat{x}_1, \hat{x}_2)$ are the estimates of the states (x_1, x_2). z_1, z_2 are the output error injections written as

$$\begin{aligned} z_1 &= \lambda \left| x_1 - \hat{x}_1 \right|^{\frac{1}{2}} \operatorname{sign}\left(x_1 - \hat{x}_1\right) \\ z_2 &= \alpha \operatorname{sign}\left(x_1 - \hat{x}_1\right) \end{aligned} \tag{13}$$

with $\lambda, \alpha \in \mathbb{R}_+$. Introducing the expressions $\tilde{x}_1 = x_1 - \hat{x}_1$ and $\tilde{x}_2 = x_2 - \hat{x}_2$, the error equations can be explicated as

$$\begin{aligned} \dot{\tilde{x}}_1 &= \tilde{x}_2 - \lambda |\tilde{x}|^{\frac{1}{2}} \operatorname{sign}\left(\tilde{x}_1\right) \\ \dot{\tilde{x}}_2 &= F(t, x_1, x_2, \hat{x}_2) - \alpha \operatorname{sign}\left(\tilde{x}_1\right) \end{aligned} \tag{14}$$

where

$$\begin{aligned} F(t, x_1, x_2, \hat{x}_2) = f(t, x_1, x_2, u) - f(t, x_1, \hat{x}_2, u) + \\ + \xi(t, x_1, x_2, u) \end{aligned} \tag{15}$$

Bounded states are required to ensure the solution convergence to the sliding surface. Thus, the existence of the constant f^+ is ensured,

$$|F(t, x_1, x_2, \hat{x}_2)| \leq f^+ \tag{16}$$

and it holds for any possible t, x_1, x_2 and $|\hat{x}_2| \leq 2 \sup |x_2|$. The parameters α, λ of the observer can be selected as $\alpha = a_1 f^+$ and $\lambda = a_2 (f^+)^{\frac{1}{2}}$, in which usually $a_1 = 1.1$ and $a_2 = 1.5$. Hence, the convergence of the observer states $(\hat{x}_1, \hat{x}_2)$ from Eq. (12) and (13) to the system state variables (x_1, x_2) occurs in finite time. Moreover, for the proposed observer, the design of the gains α and λ is based on an estimate of $F(t, x_1, x_2, \hat{x}_2, u)$ and this means that a partial knowledge of the system dynamics is taken into account.

ARTIFICIAL POTENTIAL FIELDS FOR GUIDANCE

APF founding principle consists of building an attractive potential field U_a, which creates a motion towards the goal point, while modelling the presence of obstacles as sum of repulsive potential fields $U_r = \sum U_{r_i}$, with $1, \ldots, N_{obs}$ (N_{obs} is the number of obstacles). The motion is then forced along the opposite direction of the gradient $\nabla U = \nabla (U_a + U_r)$ in order to reach the goal avoiding all the obstacles.

Classical Artificial Potential Field

The classical APF, as in Reference 13, has a paraboloid and a squared hyperbolic function as the attractive and repulsive fields, respectively.

$$U_a(r) = \frac{K_a}{2}\eta_a(r)^2, \;\; U_{r_i}(r) = \frac{K_r}{2}\left(\frac{1}{\eta_{r_i}(r)} - \frac{1}{\eta_0}\right)^2 \tag{17}$$

where $\eta_a(r) = \|r_{goal} - r\|$ is the distance of the Chaser from the goal point, with $r_{goal} \in \mathbb{R}^3$ the position vector of the goal and $r \in \mathbb{R}^3$ the position vector of the Chaser, obtained by Eq. (1). Moreover, from Eq. (17), $\eta_{r_i}(r) = \min_{\forall r_{obs_i} \in CO_i} \|r_{obs_i} - r\|$ is the minimum distance between the Chaser and the obstacles, with CO_i being the convex set of the i^{th}-obstacle points and $r_{obs} \in \mathbb{R}^3$ being the obstacle position vector, η_0 is the maximum influence distance of the obstacles, K_a and K_r are the attractive and repulsive constants.

Harmonic Artificial Potential Fields

Harmonic APFs are not affected by *local minima* problem. In this case, both the attractive and repulsive potential fields must be modelled as harmonic functions, which satisfy the Laplace equation $\nabla^2 U(r) = 0 \;\; \forall r \in \mathbb{D}$, where $\mathbb{D}$ is the domain of $U(r)$. Some features of harmonic functions are:

- *minimum and maximum principle*: the minimum and the maximum of a non constant harmonic function occur on the domain boundary.
- *invariance under linear transformations*: linear combinations of harmonic functions are still harmonic functions.

With these features, regardless of the obstacle number, the total potential field $U(r)$ is free of local minima. The difference in gradient lines of harmonic and non harmonic fields is shown in Figure 2. This approach has been already exploited for 2D robotic applications.[11,19,20] For 3D applications, the Laplace equation in polar coordinates, as in Reference 19 and neglecting angular terms, is in n-dimensions

$$\nabla^2 U(r) = U_{rr} + \frac{n-1}{r}U_r \tag{18}$$

where U_{rr} and U_r are the second and first derivative of the field U w.r.t. the position r, respectively. Integrating Eq. (18), we have

$$U(r) = \frac{c_1}{r^{n-2}} + c_2 \tag{19}$$

where c_1 and c_2 are positive constants. The hyperbolic field is, therefore, a 3D harmonic function. Starting from Reference 14, the proposed local minima-free APF algorithm is modified and built using harmonic attractive and repulsive fields as

$$\begin{aligned} U_a(r) &= -\frac{1}{\eta_a(r)} \\ U_{r_i}(r) &= \begin{cases} q_i\left(\frac{1}{\eta_{r_i}(r)} - \frac{1}{\eta_0}\right) & \text{if } \eta_{r_i} \leq \eta_0 \\ 0 & \text{otherwise} \end{cases} \end{aligned} \tag{20}$$

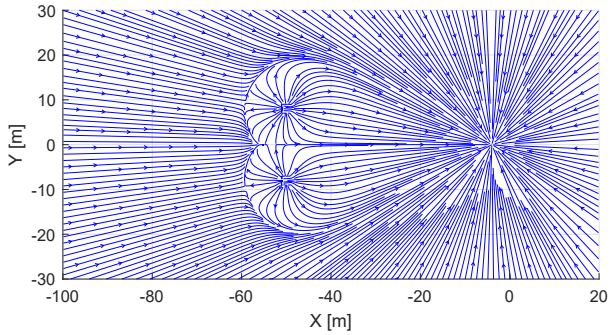

(a) Classical APF

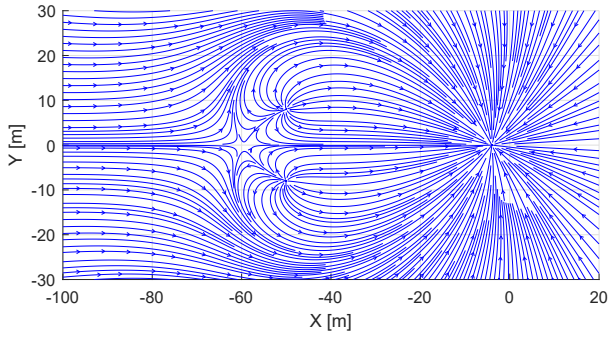

(b) Harmonic APF

Figure 2: **Example of gradient lines of APF comparison**

where $q_i = \left(\frac{R_i}{R_i+D_i}\right)^2$ is the gain of the repulsive field, η_0 is the maximum influence distance of the obstacles. $R_i = R_{s,i} + R_c$, with $R_{s,i}$ is the safety radius of the obstacles, $i = 1, \ldots, N_{obs}$, and R_c is the radius of the volumetric sphere containing the Chaser. D_i is the distance between the obstacle and the goal. The gradient of the attractive and repulsive fields is

$$\nabla_r (U_a) = -\frac{n_{CG}}{\eta_a(r)^2}, \quad \nabla_r (U_{r_i}) = q_i \frac{n_{CO_i}}{\eta_{r_i}(r)^2} \tag{21}$$

where $n_{CG} = \frac{r_{goal}-r}{\|r_{goal}-r\|}$ and $n_{CO_i} = \frac{r_{obs_i}-r}{\|r_{obs_i}-r\|}$ are the unit vectors pointing from the Chaser towards the goal and the i^{th}-obstacle, respectively.[17] The desired velocity is

$$v_{des} = \begin{cases} -\frac{\nabla_r(U(r))}{\|\nabla_r(U(r))\|} v_{mod} & \text{if } \|\nabla_r (U(r))\| \neq 0 \\ 0 & \text{otherwise} \end{cases} \tag{22}$$

where v_{mod} is the desired velocity modulus which should increase with the distance from the goal and becomes zero when the goal is reached.

Moving obstacles

In case of moving obstacles, the relative velocity between the Chaser and the obstacle is included in the algorithm. Starting from Reference 14, 17, instead of a static radius, a dynamic radius is

considered in the definition of the repulsive gain q.

$$R_{dyn_i}(r,v) = R_{s,i} + R_c + \frac{v_{R_i}(r,v)^2}{2\varepsilon a_{max}} \tag{23}$$

where $v_{R_i}(r,v) = (v - v_{obs_i})\, n_{CO_i}$ is the component of the relative velocity of the Chaser w.r.t. the i^{th}-obstacle along the unit vector n_{CO_i}, ε is a safety factor, $a_{max} = \frac{F_{max}}{\sqrt{2}m_c}$ is the maximum control acceleration with F_{max} the maximum force provided by the actuation system. The last term of Eq. (23), $\frac{v_{R_i}(r,v)^2}{2\varepsilon a_{max}}$, is actually the distance required to stop the Chaser motion w.r.t. the obstacle. The following terms are added to the repulsive gradient already formulated in Eq. (21).

$$\begin{aligned}
\nabla_r\left(U_{r_i}\right) &= \overbrace{-2\frac{R_{dyn_i}D_i}{(R_{dyn_i}+D_i)^3}\frac{v_{R_i}v_{R_{\perp i}}n_{CO_{\perp i}}}{\eta_{r_i}a_{max}}}^{\nabla_r(q_i)}\left(\frac{1}{\eta_{r_i}} - \frac{1}{\eta_0}\right) \\
\nabla_v\left(U_{r_i}\right) &= \underbrace{2\frac{R_{dyn_i}D_i}{(R_{dyn_i}+D_i)^3}\frac{v_{R_i}}{a_{max}}n_{CO_i}}_{\nabla_v(q_i)}\left(\frac{1}{\eta_{r_i}} - \frac{1}{\eta_0}\right)
\end{aligned} \tag{24}$$

where $v_{R_{\perp i}}n_{CO_{\perp i}}$ is the component of the Chaser relative velocity w.r.t. the i^{th}-obstacle perpendicular to the unit vector n_{CO_i}. The additional gradient terms reported in Eq. (24) reinforce the repulsive effect in the $-n_{CO_i}$ direction and add a steering effect along $n_{CO_{\perp i}}$ to circumnavigate the object. Further information about how to obtain such terms can be found in Reference 17.

The approach previously described can be applied even with fixed obstacles to augment the safety of the maneuver. In this case, R_{dyn_i} is considered only in the definition of the repulsive gain q_i, while the repulsive gradient terms introduced in Eq. (24) are neglected in order not to drive the Chaser too far away from the obstacle.

Moving targets

In Reference 17, the attractive field takes into account also the relative velocity of the Chaser w.r.t. the goal, to make the robot follow a desired trajectory. Instead, in our work, the modulus v_{mod} of the desired speed in Eq. (22) is simply evaluated as

$$v_{mod}(r,t) = \|v_{goal}(t)\| + \Delta v_{plus}\eta_a(r) \tag{25}$$

where Δv_{plus} is the magnitude of the relative velocity of the Chaser w.r.t. the desired goal when $\eta_a(r) = \|r_{goal} - r\| = 1$ m. The attractive field attracts the Chaser towards the moving goal and the higher the relative distance is, the faster the spacecraft is w.r.t. the target point. So, the Chaser is able to reach the goal with zero relative velocity.

Moreover, in presence of both obstacles and moving targets, the attractive gradient modulus must be resized before summing it with the repulsive one when the distance D_i between the goal point and the i^{th}-obstacle is less than R_{dyn_i}. Otherwise, the Chaser is guided by the goal point inside the safety sphere of the obstacle. Thus, the attractive gradient w.r.t. position is resized as

$$\nabla_r(U_a) = \frac{\nabla_r(U_a)}{\|\nabla_r(U_a)\|}\|\nabla_r(U_{r_i})\|. \tag{26}$$

where $\|\nabla_r(U_a)\| \neq 0\ \forall r \in \mathbb{D}_{U_a}$ since $U_a(r)$ is an harmonic function.

SLIDING MODE TECHNIQUE FOR CONTROL

In order to follow the desired velocity vector provided by the harmonic APF algorithm, a standard first-order Sliding Mode Controller (SMC) is selected. Thanks to its ability to reduce high dimensional problems into sub-tasks of lower dimensionality, the SMC allows true decoupling of the tasks "design of the potential field" and " tracking the gradient", being theoretically able to track any smooth artificial vectors field. The control law is described as[13,14]

$$F_{thr} = -F_{max}\,\mathrm{sign}\left(\hat{v} - v_{des}\right), \tag{27}$$

where $\hat{v}, v_{des} \in \mathbb{R}^3$ represent respectively the velocity estimated by the navigation algorithm and the desired velocity vector computed by the APF. This formulation forces a sliding motion onto the sliding surface $\mathcal{S} = \{\hat{v} \ \in \mathbb{R}^3 : \ \hat{v} - v_{des} = 0\}$ and reproduces with good approximation the ON/OFF behaviour of the actuation system (i.e. thrusters with maximum thrust F_{max}). Constant application of the SMC, however, would lead to an excessive propellant consumption, due to the switching behavior characterizing the sign function once convergence is achieved. For this reason, the control law expressed in Eq. (27) is activated following the law

$$F_{thr} = \begin{cases} -F_{max}\,\mathrm{sign}\left(\hat{v} - v_{des}\right) & \text{if } \|\hat{v} - v_{des}\| \geq \Delta v_{act} \\ 0 & \text{otherwise} \end{cases} \tag{28}$$

where Δv_{act} is a parameter setting the maximum velocity discrepancy accepted and should be chosen following a trade-off process. High values of Δv_{act}, in fact, would lead to great reduction of fuel consumption but would strongly deteriorate the SMC ability to track the APF velocity vectors field.

SIMULATION RESULTS

In this section the results of numerical simulations are shown. First, the analyzed maneuver is described, to clearly understand the initial conditions in terms of positions and velocities. Second, the navigation algorithm performance are analyzed. The performance of these algorithms are tested including only the Hill's Equations. Finally, we analyze the APF behavior when coupled with the standard SMC previously described to form a closed-loop and operate with moving obstacles.

Maneuver description and Chaser configuration

The navigation and guidance algorithms are tested in simulations in a rendezvous maneuver, including the closing and final approach phases. The Target is orbiting on a 400 km-height orbit. The closing phase, starting from about -500 m and ending at -100 m on V_{bar}, consists of two consecutive radial boosts, for safety aspects.[10] Lastly, the final approach consists of a straight line towards the Target starting from about -100 m on V_{bar} and ending 4 m behind the Target. Obstacles are taken into account in both phases.

For the Chaser configuration, a 1500 kg-satellite (with $R_c = 2\ m$) equipped as reported in Table 1 and 2 is considered. The spacecraft Body frame is considered to be aligned with the LVLH frame during the entire maneuver and two thrusters are simultaneously switched on along each axis.

Navigation algorithm performance

The performance of both observers are tested in the first minutes of simulation for the radial boost phase. The Chaser starts at $r = [-500,\ 0,\ 0]^T$ m with zero velocity in the LVLH frame. The initial

Table 1: **Thrusters features**

Cluster	**Thruster type**	**Maximum Thrust F_{max}**
12 thrusters (2 along each axis direction)	Thermochemical	20 N

Table 2: **Sensors features**

Sensor	**Sample rate**	**Noise**
Optical camera	10 Hz	1% of the range - White-Gaussian
Acceleromter	100 Hz	4 mg - White-Gaussian

conditions of the observers at $t = 0$ s are $\hat{r}(0) = [-510, 20, -10]^T$ m and $\hat{v}(0) = [V_{x,0}, 0, 0]^T$ m/s, where $V_{x,0} = \frac{3}{2}\omega\Delta\hat{z}$, with $\Delta\hat{z} = -10$ m difference between the Chaser and Target orbits. Note that in the simulated maneuver, the Chaser starts at the same orbit of the Target, instead, in the observer initial conditions, we assume a different initial orbit to evaluate the estimation performance of the observer. In this section, navigation algorithms are executed at a frequency of 10 Hz to test their performance at low operational frequencies.

Firstly, linear robust SMO results are shown in Figure 3. The simulation parameters of the observer are selected as $\rho = 22$, $G = \mathrm{diag}(0.005, 0.005, 0.005, 0.5, 0.5, 0.5)$, $P = \mathrm{diag}(5, 5, 5, 746.5, 746.5, 746.5)$, $F = [0_{3\times3}, 0.5 \cdot I_{3\times3}]$, i.e. the algorithm is able to withstand an unknown input up to more than 20 N. As stated before, the first-order SMO requires both position and velocity measurements as inputs. The position is provided by the optical camera sensor, instead the velocity is obtained by the combination (i.e. data fusion) of the camera and the accelerometer measurements.

The STW-SMO algorithm has the same initial conditions of the linear observer, however the observation of the variables can be performed with a partial set of information, requiring just the knowledge of position measurements. Since both the velocity and position vectors from the accelerometers are obtained by integration, a measurement drift can be observed. For this reason, the close range camera position is used to reset the error at each second.

Moreover, we set $f^+ = 1$, $\alpha = a_1 f^+$ and $\lambda = a_2, (f^+)^{\frac{1}{2}}$, with $a_1 = 1.1$ and $a_2 = 1.5$. Additive White Gaussian Noise (AWGN) of both accelerometer and close range camera measurements are included in the simulations. The simulation results are shown in Figure 4.

If the results of both Figure 3 and 4 are analyzed, although both observers converge in finite time, the STW-SMO achieves the convergence faster than the linear SMO. In particular, the velocity estimation requires about 30 s for the first-order observer and about 5 s for the second-order one. Moreover, smaller is the initial estimate error, faster is the achievement of the convergence. Analyzing the accuracy of both algorithms, Figure 5 shows the position residual error of both observers. The simulation time is selected to analyze the behaviour once both the observers have reached the convergence. A residual error of about 10^{-4} m is evaluated for the STW-SMO, compared with 10^{-1} m of the first-order SMO. However, as shown in Figure 6, the velocity residual error for the first-

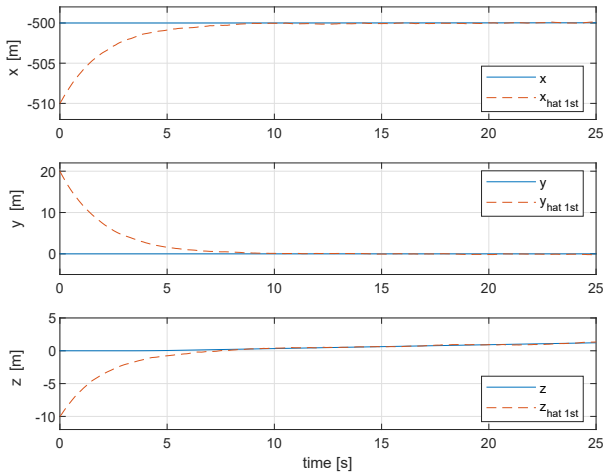

(a) Position vector x estimation

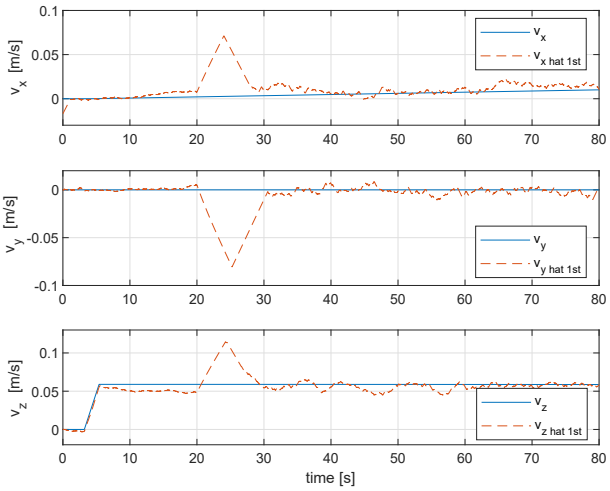

(b) Linear velocity v estimation

Figure 3: **Simulation results of the 1^{st} order-SMO variables estimation**

order SMO is less affected by chattering behavior. For this reason, a combination of both observers is proposed: (i) the position vector can be estimated by SWT-SMO observer and (ii) the velocity vector from the first-order SMO.

Remark 1 *From Figure 5 and 6 it is possible to notice that the first-order robust SMO is characterized by a lower frequency chattering behavior. This is caused by the presence of both linear and discontinuous feedback correction term in its formulation, Eq. (7).*

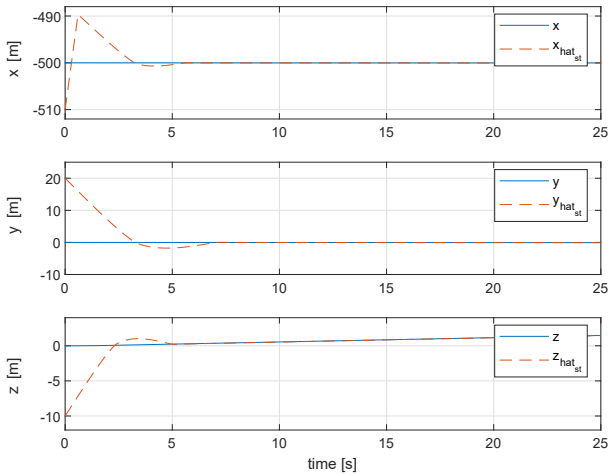

(a) Position vector x estimation

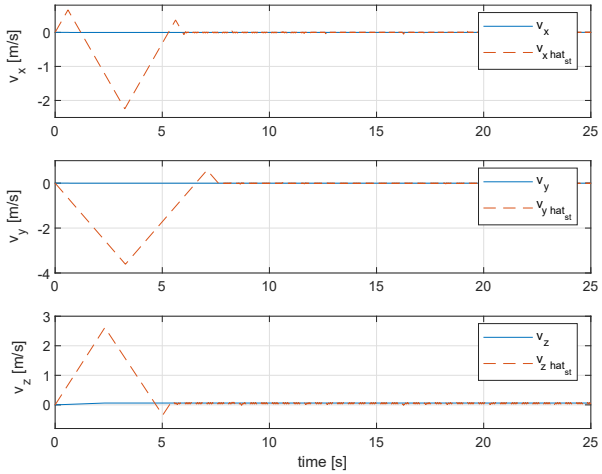

(b) Linear velocity v estimation

Figure 4: **Simulation Results of the STW-SMO variables estimation**

Remark 2 *The accuracy of both observers increases when the Chaser is approaching the Target, due to the reduction of the camera measurement noise, achieving an accuracy on the velocity estimates of about* 10^{-3} *m/s in the last* 100 *m.*

Remark 3 *Even if the STW-SMO for the velocity estimation is less accurate than the first-order SMO, if some measurements are not available, the second-order algorithm is able to estimate both position and velocity vectors. Instead, the linear robust SMO needs the measurement of both* $\hat{r}$ *and* $\hat{v}$ *variables for estimation and* $C = I_{p\times n}$ *with* $p = n$ *is required in order to solve the LMI in Eq. (8), (9) and (10). Thus, if a failure occurs, only STW-SMO is able to estimate both variables.*

Finally, a comparison with an Extended Kalman Filter (EKF) is proposed. Note that the EKF is

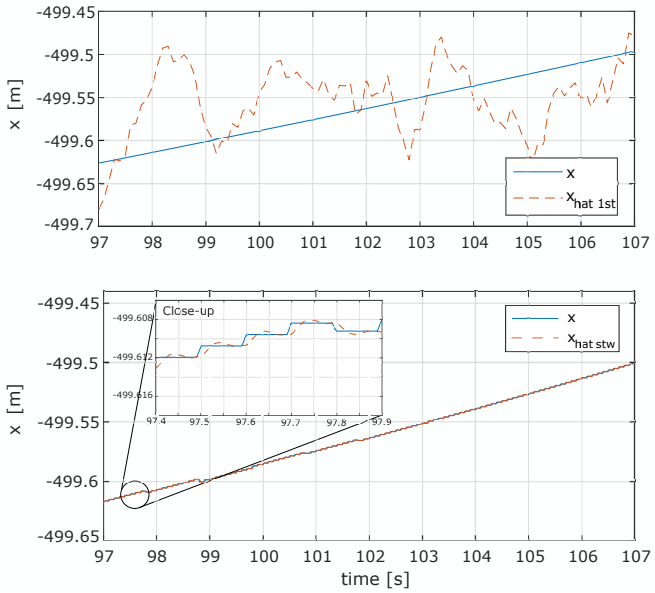

Figure 5: **Position residual errors of Linear Robust SMO and STW-SMO**

used for linear or linearized processes and measurements systems. In our case, the system in Eq. (2) is used for the filter definition and to obtain an optimal estimation of the system states. Initial value tuning is one of the key problems of EKF. Thus, EKF is not robust w.r.t. the external disturbances and measurement noise, and covariance matrices are required for accurate evaluation of noise. The

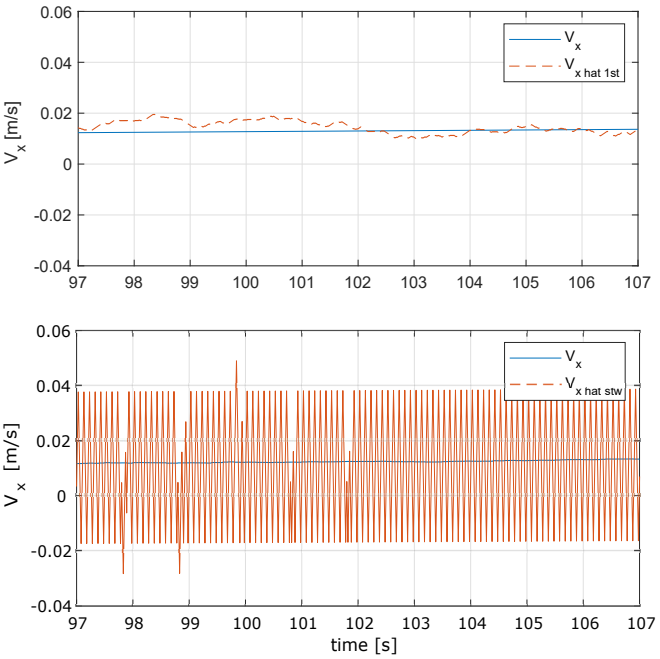

Figure 6: **Velocity residual errors of Linear Robust SMO and STW-SMO**

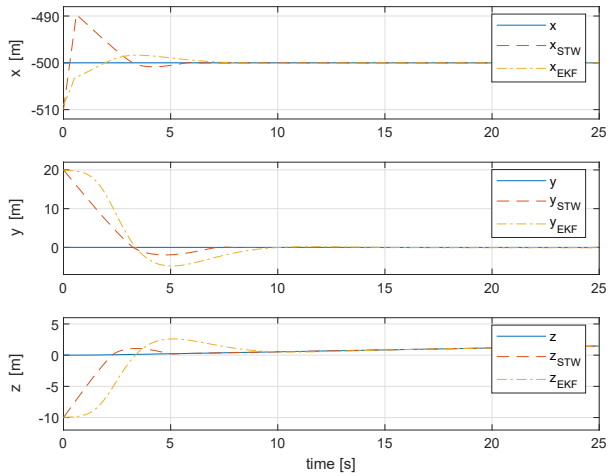

Figure 7: Comparison between STW-SMO and EKF in position observation

comparison between the two algorithms is performed at a frequency of 10 Hz and with the same initial conditions. As in Figure 7, though EKF is an effective and well known technique, STW-SMO can be a valid alternative even at low operational frequencies and even considering the chattering drawback.

Closed-loop GNC Simulation Results

In this section, the closed-loop GNC system in Figure 8 is considered in which: (i) the dynamics is based on Hill's equations as in Eq. (1) and from the sensor block it is possible to get the measured state, with a White Gaussian Noise introduced in the analysis, in terms of position $r_{meas} = [\mathrm{x_{meas}}, \mathrm{y_{meas}}, \mathrm{z_{meas}}]^T$ and velocity $v_{meas} = [v_{x_{meas}}, v_{y_{meas}}, v_{z_{meas}}]^T$ components, (ii) the navigation block, in which linear robust SMO and STW-SMO are combined as previously explained, is able to estimate both correct position and velocity of the Chaser, (iii) the guidance algorithm is the harmonic APF discussed in previous sections, which allows to follow the desired trajectory while performing obstacle avoidance, and (iv) the control function is executed by the the first-order SMC (discontinuously activated with $\Delta v_{act} = 0.03\ m/s$ during the closing phase and $\Delta v_{act} = 0.005\ m/s$ in the final approach), which provides the value of thrust needed to accom-

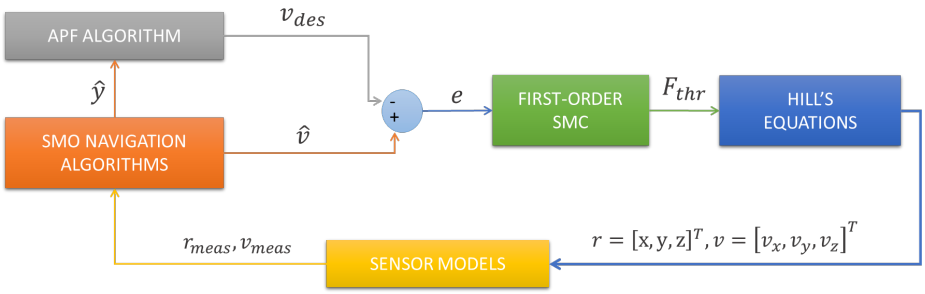

Figure 8: Closed-loop GNC scheme

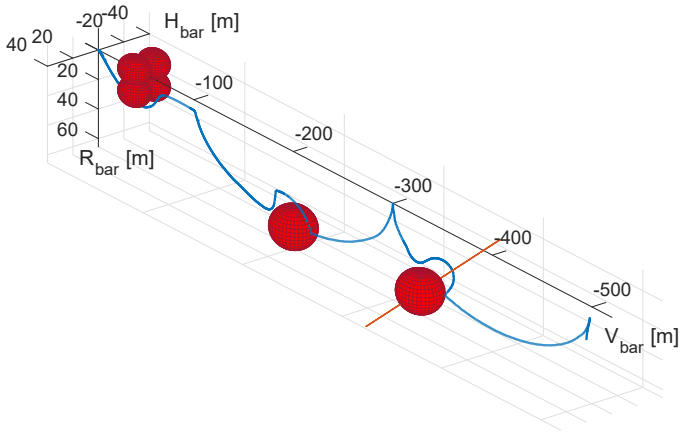

Figure 9: **Closed-loop maneuver execution with obstacles safety ellipsoids in red**

plish the maneuver described in the "Maneuver description and Chaser configuration" subsection. This value represents the input variable $u \in \mathbb{R}^m$ in the state-space formulation. In order to test the robustness of the combined SMOs, only half of the thrust magnitude information is provided to the navigation block, artificially creating an uncertainty in the system. Moreover, to show the effectiveness of the APF algorithm in presence of obstacles, ellipsoid obstacles (physical semi-axes $5,\ 2.5,\ 2.5$ m) are included in the simulation environment. The Hill dynamics and observer initial conditions are selected as

$$\begin{aligned} r(0) &= [-520; 20; 10]\ \ m,\ v(0) = \left[\frac{3}{2}\,\omega\Delta \mathrm{z}; 0; 0\right]\ \ \frac{m}{s} \\ \hat{r}(0) &= [-500; 0; 0]\ \ m,\ \hat{v}(0) = [0; 0; 0]\ \ \frac{m}{s} \end{aligned} \tag{29}$$

to simulate position errors due to previous rendezvous phases, not included here. Navigation algorithms are executed at 100 Hz, while Guidance and Control ones at 10 Hz. The Chaser encounters two obstacles during the closing phase, the first one moving near the end of the first radial boost and the second fixed in the middle of the second maneuver. The safety radius considered during this phase is $R_s = 10$ m. In the final approach, instead, four fixed obstacles with safety radius of $R_s = 5$ m are located at $\mathrm{x} = -50$ m and $\mathrm{y} = \pm 7.5$ m, two of them placed at $\mathrm{z} = 10$ m, the others at $\mathrm{z} = -5$ m. Note that this configuration is selected since, with classical APF, local minima should be found. Instead, the Chaser is able to perform the maneuver thanks to harmonic APF functions. Simulations results are shown in Figure 9.

Lastly, Figure 10 shows examples of different paths the Chaser could follow to avoid the final four obstacles, clearly showing a three-dimensional saddle point. So, different trajectories can be followed by the Chaser, without encountering local minima and avoiding the obstacles.

CONCLUSIONS

In this paper both Navigation and Guidance algorithms have been introduced, testing their effectiveness in space missions applications. As navigation algorithms, two Sliding Mode Observers (SMO) are proposed, for the estimation of the positions and velocities. Both the proposed SMOs have peculiar features and the combination of these two algorithms is shown to be robust and effective for the selected maneuver. Moreover, a comparison with Extended Kalman Filter (EFK)

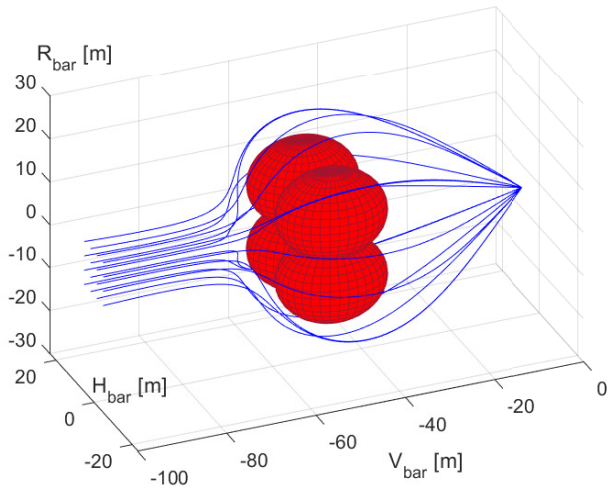

Figure 10: **Possible paths to avoid a group of obstacles**

shows that SMO algorithms represent valid alternatives. As Guidance algorithms, harmonic 3D Artificial Potential Field (APF) functions are designed to overcome the local minima problem, including moving obstacles and targets. The method used for the definition of the dynamic radius of the obstacles and of the repulsive gain includes both the Chaser and either moving or fixed convex obstacles. The combination of the proposed Navigation and Guidance algorithms has shown operational effectiveness, achieving a level of accuracy suitable for rendezvous maneuvers. Finally, a closed-loop maneuver with a discontinuously activated Sliding Mode Controller (SMC) shows the effectiveness and robustness of the proposed algorithm combination, including the typical actuation system behaviour.

REFERENCES

[1] P. S. Maybeck, *The Kalman Filter: An Introduction to Concepts*, pp. 194–204. New York, NY: Springer New York, 1990.

[2] M. S. A. Adnane, A. Bellar and Z. Ahmed Foitih, "Spacecraft Attitude Estimation Based on Star Tracker and Gyroscope Sensors," *International Conference on Automatic Control, Telecommunications and Signals*, 2015.

[3] S. K. Spurgeon, "Sliding mode observers: a survey," *International Journal of Systems Science*, Vol. 39, No. 8, 2008, pp. 751–764.

[4] C. Edwards, S. K. Spurgeon, and C. P. Tan, *On the Development and Application of Sliding Mode Observers*, pp. 253–282. Berlin, Heidelberg: Springer Berlin Heidelberg, 2002.

[5] Y. Zhang, Z. Zhao, T. Lu, L. Yuan, W. Xu, and J. Zhu, "A comparative study of Luenberger observer, sliding mode observer and extended Kalman filter for sensorless vector control of induction motor drives," *2009 IEEE Energy Conversion Congress and Exposition*, 2009, pp. 2466–2473, 10.1109/ECCE.2009.5316508.

[6] Changsheng Li and M. Elbuluk, "A sliding mode observer for sensorless control of permanent magnet synchronous motors," *Conference Record of the 2001 IEEE Industry Applications Conference. 36th IAS Annual Meeting (Cat. No.01CH37248)*, Vol. 2, 2001, pp. 1273–1278 vol.2, 10.1109/IAS.2001.955672.

[7] H. Majid and H. Abouaïssa, "Comparative Study of a Super-Twisting Sliding Mode Observer and an Extended Kalman Filter for a Freeway Traffic System," *Cybernetics and Information Technologies*, Vol. 15, No. 2, 01 Jun. 2015, pp. 141 – 158, https://doi.org/10.1515/cait-2015-0034.

[8] I. Schkolnikov, Y. Shtessel, P. Zarchan, and D. Lianos, "Sliding Mode Observers Versus Kalman Filter in the Homing Loop," 07 2001, p. 8.

[9] K. Koprubasi and M. . L. Thein, "Spacecraft attitude and rate estimation using sliding mode observers," *International Conference on Recent Advances in Space Technologies, 2003. RAST '03. Proceedings of*, 2003, pp. 165–170, 10.1109/RAST.2003.1303901.

[10] W. Fehse, *Automated rendezvous and docking of spacecraft*. Cambridge University Press, 2003.

[11] A. Ferrara and M. Rubagotti, "Second-order sliding-mode control of a mobile robot based on a harmonic potential field," *Control Theory & Applications, IET*, Vol. 2, 10 2008, pp. 807 – 818, 10.1049/iet-cta:20070424.

[12] R. Zappulla, H. Park, J. Virgili-Llop, and M. Romano, "Real-Time Autonomous Spacecraft Proximity Maneuvers and Docking Using an Adaptive Artificial Potential Field Approach," *IEEE Transactions on Control Systems Technology*, Vol. 27, No. 6, 2019, pp. 2598–2605, 10.1109/TCST.2018.2866963.

[13] N. Bloise, E. Capello, M. Dentis, and E. Punta, "Obstacle Avoidance with Potential Field Applied to a Rendezvous Maneuver," *Applied Sciences*, Vol. 7, No. 10, 2017.

[14] M. Mancini, N. Bloise, E. Capello, and E. Punta, "Sliding Mode Control Techniques and Artificial Potential Field for Dynamic Collision Avoidance in Rendezvous Maneuvers," *IEEE Control Systems Letters*, Vol. 4, No. 2, 2020, pp. 313–318, 10.1109/LCSYS.2019.2926053.

[15] L. Zhou and W. Li, "Adaptive Artificial Potential Field Approach for Obstacle Avoidance Path Planning," *2014 Seventh International Symposium on Computational Intelligence and Design*, Vol. 2, 2014, pp. 429–432, 10.1109/ISCID.2014.144.

[16] S. M. Hosseini Rostami, A. Kumar, J. Wang, and X. Liu, "Obstacle avoidance of mobile robots using modified artificial potential field algorithm," *EURASIP Journal on Wireless Communications and Networking*, Vol. 2019, 03 2019, 10.1186/s13638-019-1396-2.

[17] S. Ge and Y. Cui, "Dynamic Motion Planning for Mobile Robots Using Potential Field Method," *Autonomous Robots*, Vol. 13, 11 2002, pp. 207–222, 10.1023/A:1020564024509.

[18] Y. Shtessel, C. Edwards, L. Fridman, and A. Levant, *Sliding mode control and observation*. Springer Science+Business Media, New York, 2014.

[19] J. Kim and P. K. Khosla, "Real-time obstacle avoidance using harmonic potential functions," *IEEE Transactions on Robotics and Automation*, Vol. 8, No. 3, 1992, pp. 338–349, 10.1109/70.143352.

[20] J. Guldner and V. I. Utkin, "Sliding mode control for gradient tracking and robot navigation using artificial potential fields," *IEEE Transactions on Robotics and Automation*, Vol. 11, No. 2, 1995, pp. 247–254.